Brittle creep in basalt and its application to time-dependent volcano deformation

M.J. Heap [a,b,*], P. Baud [b], P.G. Meredith [a], S. Vinciguerra [c], A.F. Bell [d], I.G. Main [d]

[a] Rock and Ice Physics Laboratory (RIPL), Department of Earth Sciences, University College London, Gower Street, London WC1E 6BT, UK
[b] Laboratoire de Géophysique Expérimentale, Institut de Physique de Globe de Strasbourg (UMR 7516 CNRS, Université de Strasbourg/EOST), 5 rue René Descartes, 67084 Strasbourg cedex, France
[c] Istituto Nazionale di Geofisica e Vulcanologia, Sezione di Roma1, Via di Vigna Murata 605, 00143, Rome, Italy
[d] School of GeoSciences, The University of Edinburgh, Grant Institute, The King's Buildings, West Mains Road, Edinburgh, EH9 3JW, UK

ABSTRACT

Time-dependent brittle deformation is a fundamental and pervasive process operating in the Earth's upper crust. Its characterization is a pre-requisite to understanding and unraveling the complexities of crustal evolution and dynamics. The preferential chemical interaction between pore fluids and strained atomic bonds at crack tips, a mechanism known as stress corrosion, allows rock to fail under a constant stress that is well below its short-term strength over an extended period of time; a process known as brittle creep. Here we present the first experimental measurements of brittle creep in a basic igneous rock (a basalt from Mt. Etna volcano) under triaxial stress conditions. Results from conventional creep experiments show that creep strain rates are highly dependent on the level of applied stress (and can be equally well fit by a power law or an exponential law); with a 20% increase in stress producing close to three orders of magnitude increase in creep strain rate. Results from stress-stepping creep experiments show that creep strain rates are also influenced by the imposed effective confining pressure. We show that only part of this change can be attributed to the purely mechanical influence of an increase in effective pressure, with the remainder interpreted as due to a reduction in stress corrosion reactions; the result of a reduction in crack aperture that restricts the rate of transport of reactive species to crack tips. Overall, our results also suggest that a critical level of crack damage is required before the deformation starts to accelerate to failure, regardless of the level of applied stress and the time taken to reach this point. The experimental results are discussed in terms of microstructural observations and fits to a macroscopic creep law, and compared with the observed deformation history at Mt. Etna volcano.

© 2011 Elsevier B.V. All rights reserved.

1. Introduction

The presence of a fluid phase in cracks within rock is known to have both a mechanical and a chemical influence on deformation characteristics. Mechanically, pressurized pore fluids reduce all the applied normal stresses equally and thus allow rocks to fail at lower applied differential stress (σ_1–σ_3, henceforth termed 'Q') than would otherwise be the case (Jaeger et al., 2007; Terzaghi, 1943). Chemically, the presence of a pore fluid phase reduces the surface free energy as the result of the absorption onto the internal pore surfaces (Andrade and Randall, 1949; Orowan, 1944; Rehbinder, 1948), and also promotes time-dependent, subcritical crack growth, of which stress corrosion is the most important mechanism in the Earth's brittle upper crust (Anderson and Grew, 1977; Atkinson, 1984a, 1984b; Atkinson and Meredith, 1987; Costin, 1987).

Stress corrosion is a process by which strained atomic bonds at crack tips react preferentially with the chemically active pore fluid; commonly water or some aqueous solution in the upper crust. This allows cracks to propagate at much lower stresses than would otherwise be expected (Freiman, 1984; Hadizadeh and Law, 1991; Michalske and Freiman, 1982). Crack propagation rates are controlled by the level of stress intensity at crack tips (a function of both applied stress and crack length), and will increase as cracks extend even under a constant stress.

Double-torsion fracture mechanics experiments have provided much information on the growth of tensile macrocracks in rock by the process of stress corrosion (see Atkinson, 1984a, 1984b; Atkinson and Meredith, 1987 for reviews). However, whilst many studies have concentrated on quartz-rich rocks such as sandstones and granites, only very few studies have reported measurements on basic igneous rocks such as basalts, dolerites and gabbros (Meredith and Atkinson, 1983, 1985; Swanson, 1984; Waza et al., 1980) and intermediate igneous rocks such as andesites (Jeong et al., 2007; Nara and Kaneko, 2005; Nara et al., 2010). All of these studies demonstrate that subcritical crack propagation occurs in basic and intermediate rocks in the presence of water. In particular, Meredith and Atkinson (1985) and Nara and

* Corresponding author at: Laboratoire de Géophysique Expérimentale, Institut de Physique de Globe de Strasbourg (UMR 7516 CNRS, Université de Strasbourg/EOST), 5 rue René Descartes, 67084 Strasbourg cedex, France.
E-mail address: m.heap@ucl.ac.uk (M.J. Heap).

Kaneko (2005) showed that the rate of crack growth increased with increasing partial pressure of water or water vapor. The most widely used and accepted theory relating the rate of crack growth to the stress concentration at the crack tip during stress corrosion is Charles' power law (Charles, 1958), which has been used to describe virtually all experimentally determined data for geological materials (see Atkinson, 1984a, 1984b; Meredith and Atkinson, 1983; Swanson, 1984). However, exponential forms, such as the Charles–Hillig–Wiederhorn theory (Hillig and Charles, 1965; Wiederhorn and Bolz, 1970), have so far been shown to describe creep behavior equally as well over the range of data achievable in the laboratory (see Costin, 1987; Heap et al., 2009a; Lawn, 1993; Lockner, 1993; Ngwenya et al., 2001).

Whilst the overwhelming majority of experimental data on stress corrosion cracking in basic rocks have been derived for single, tensile cracks propagating under ambient pressure conditions, the behavior of bulk rock deforming subjected to compressive stresses remains poorly understood. To date, studies on quartz-rich rocks loaded in triaxial compression have demonstrated that samples can deform and eventually fail under a constant Q over extended periods of time; a phenomenon known as *brittle creep* (for sandstones see Baud and Meredith, 1997; Heap et al., 2009a, 2009b; Lockner and Byerlee, 1977; Ngwenya et al., 2001; Tsai et al., 2008; Yang and Jiang, 2010; for granites see Fujii et al., 1999; Katz and Reches, 2004; Kranz, 1980; Kranz et al., 1982; Kurita et al., 1983; Lockner, 1993; Lockner and Byerlee, 1986; Maranini and Yamaguchi, 2001; Wu and Thomsen, 1975). Rocks deforming in this manner generally exhibit trimodal creep behavior when strain is plotted against time; (1) primary or transient, decelerating creep, (2) secondary, constant strain-rate creep, and (3) tertiary, accelerating creep. A physical basis for this trimodal behavior has been provided by an empirical constitutive law based on Arrhenius reaction rate equations (Lockner, 1998), mean field damage mechanics modeling that invokes a two stage process: (1) a phase of strain hardening involving distributed crack damage, and (2) a phase of strain softening involving crack interaction and coalescence (Heap et al., 2009a; Main, 2000), finite element modeling (Armitrano and Helmstetter, 2006), and viscoelastic damage rheology modeling (Hamiel et al., 2006).

However, the occurrence of time-dependent, brittle creep in basic igneous rock, such as basalt, remains unreported. This demands new investigation, especially since stress corrosion has been invoked as a potential mechanism responsible for the time-dependent precursory cracking, ground deformation and accelerating seismic activity within volcanic edifices that commonly precedes volcanic eruptions (Chastin and Main, 2003; Cornelius and Scott, 1993; Kilburn, 2003; Kilburn and Voight, 1998; Main, 1999; McGuire and Kilburn, 1997; Voight, 1988, 1989). It has been postulated that the final stages of magma ascent are controlled by the slow fracture of the rock between the magma body and the surface (Kilburn, 2003; McGuire and Kilburn, 1997; Smith and Kilburn, 2010). High stresses, caused by magma overpressure and dyke intrusion, promote the initiation and slow propagation of cracks within the surrounding rock. At a critical crack density, i.e. when cracks can interact and coalesce, the rate of cracking accelerates until the country rock 'fails', thus forming a new pathway for magma to reach the surface. This acceleration in cracking is evidenced by an acceleration in the number of volcano-tectonic (VT) seismic events recorded at volcanoes (e.g. Palano et al., 2009; Smith and Kilburn, 2010). Time-dependent brittle creep, driven by stress corrosion cracking, is a primary candidate for facilitating this precursory slow fracture. The detailed understanding of this process in volcanic rocks could therefore improve volcanic eruption forecasting and hazard mitigation.

We therefore present results from the first experimental study of brittle creep in a porphyritic, intermediate alkali basalt, the most representative lithology for intraplate and oceanic island volcanism (Wilson, 1989). Our chosen test material is a well-characterized basalt (see Benson et al., 2007, 2008; Heap et al., 2009c; Stanchits et al., 2006; Vinciguerra et al., 2005) that forms a significant proportion of the lava flow pile comprising the upper part of the edifice of Mt. Etna

volcano, a large stratovolcano situated near the eastern (Ionian) coast of Sicily (Italy). Additionally, Mt. Etna volcano represents a near-ideal candidate for our study: (1) Over the last 20 years, new technological developments and denser monitoring networks have provided one of the highest quality volcanological, geophysical and geochemical data sets for any volcano in the world (Bonaccorso et al., 2004). Mt. Etna therefore provides the highest potential for the comparison of field data and new laboratory data. (2) The shallow lava flow basalts present at Mt. Etna (0–2 km) are commonly porous and highly permeable (Vinciguerra et al., 2005) due to their fractured, and sometimes scoriaceous nature. The volcano therefore hosts a large reservoir of water (Ogniben, 1966), an essential prerequisite for subcritical crack growth by stress corrosion. (3) The edifice at Mt. Etna is considered structurally unstable and susceptible to flank collapse (Walter et al., 2005). Indeed, there is a continuous large-scale ESE seaward sliding of its eastern flank (e.g. Bonforte and Puglisi, 2003, 2006; Borgia et al., 1992, 2000; Palano et al., 2008, 2009; Rust et al., 2005). This movement is accompanied, and accelerated, by repeated episodes of brittle deformation, monitored in terms of ground deformation and seismicity (of variable duration, from days to months), linked to the intrusion of magma (Allard et al., 2006). Crucially, no direct evidence for a décollement surface, driving large-scale deformation, has been found up to now. This suggests that the time-dependent deformation of edifice-forming rocks could play a role in assisting the observed large-scale deformation.

We first introduce the investigated material and explain the experimental techniques. We then present results from constant strain rate experiments and conventional brittle creep experiments, before showing the influence of effective confining pressure on brittle creep in our basalt samples using stress-stepping creep experiments. Finally, we show microstructural observations of cracking during creep deformation, the results of fitting a macroscopic creep law to the experimental data, and a comparison with observed temporal deformation data from Mt. Etna volcano.

2. Material investigated

The material used throughout this study was a lava flow basalt from Mt. Etna volcano, collected from the southern flank of the volcano (see Fig. 1 in Heap et al., 2009c). It is a porphyritic, intermediate alkali basalt, the most representative lava flow basalt found at Mt. Etna (Tanguy et al., 1997). It has a bulk density of 2.86 g cm^{-3}, a connected porosity of 4.2% and is composed of crystals of feldspar (25%), pyroxene (8.5%) and olivine (4%) within a fine-grained groundmass (~60%) of the same materials. The physical properties of EB are summarized in Table 1.

The 'as-collected' Etna basalt (hereinafter called EB) contains an extensive pre-existing network of isotropically distributed micro-cracks considered to be of thermal origin and resulting from rapid cooling of the lava flow (Vinciguerra et al., 2005). This has resulted in anomalously low P-wave velocities at ambient pressure of 3.28 km s^{-1} for dry samples of EB, and an anomalously high permeability of 0.25×10^{-15} m^2 measured at 30 MPa effective pressure (Vinciguerra et al., 2005). All samples were taken from a similar block of EB to that used in Heap et al. (2009c). Samples were cored to a diameter of 40 mm, cut to a length of 100 mm and ground flat and parallel to within ± 0.02 mm. Samples were then vacuum-saturated with distilled water for 48 h prior to experimentation.

3. Experimental methodology

All experiments were performed under drained conditions in the large volume servo-controlled triaxial rock deformation apparatus in the Rock & Ice Physics Laboratory (RIPL) at University College London. Axial strain was monitored continuously using LVDT displacement transducers, and porosity change was measured continuously by

Table 1
The physical properties of Etna basalt.

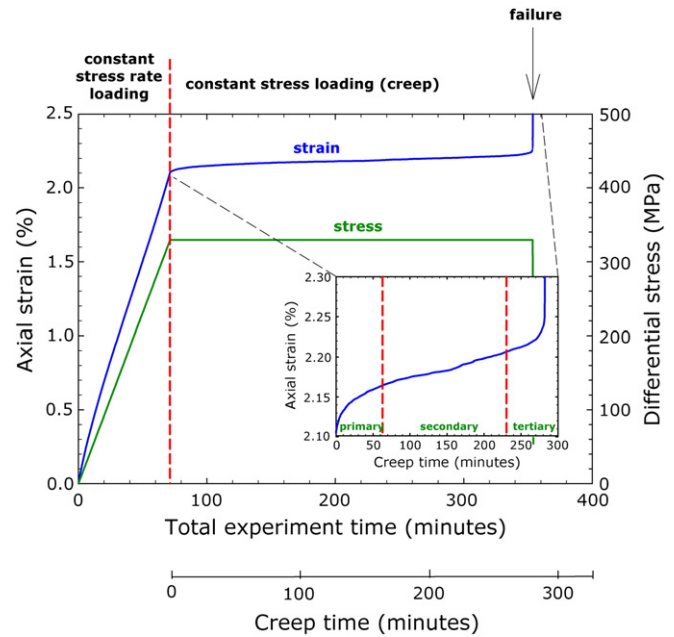|	Effective confining pressure (MPa)		Reference
Porosity (%)	0	4.2	This study
Density (g cm^3)	0	2.86	This study
Dry P-wave velocity (km s^{-1})	0	3.28	This study
Wet P-wave velocity (km s^{-1})	0	5.24	This study
Dry S-wave velocity (km s^{-1})	0	1.87	This study
Wet S-wave velocity (km s^{-1})	0	2.15	This study
Dry Vp/Vs ratio	0	1.75	This study
Wet Vp/Vs ratio	0	2.58	This study
Dry dynamic Young's modulus (GPa)	0	25.2	This study
Wet dynamic Young's modulus (GPa)	0	33.8	This study
Dry dynamic Poisson's ratio	0	0.26	This study
Wet dynamic Poisson's ratio	0	0.41	This study
Static Young's modulus (GPa)	10	17.9	This study
	20	19.1	This study
	30	21.1	This study
Permeability (m^2)	10	0.55×10^{-15}	Vinciguerra et al. (2005)
	20	0.25×10^{-15}	Vinciguerra et al. (2005)
	30	0.175×10^{-15}	Vinciguerra et al. (2005)

Fig. 1. Strain–time and stress–time plot from a conventional creep experiment on EB illustrating the experimental protocol. The experiment is divided into two phases: an initial constant stressing rate phase and a constant stress (creep) phase. The inset shows a zoomed-in view of the constant stress phase. The three creep phases (primary, secondary and tertiary) are labeled on the inset.

means of a servo-controlled pore fluid volumometer. Acoustic emission (AE) output was recorded using two PZT-5A transducers (3 mm in diameter and with 1 MHz longitudinal resonant frequency) mounted on steel inserts embedded within the rubber sample jacket, and stored by a Vallen AMSY-5 AE recording system. The change in sample porosity and the cumulative output of AE energy (the summed areas under each waveform) during deformation were recorded, in addition to axial strain, as different proxy measures of the change in "damage" during sample deformation. Porosity change records the total change in crack and pore volume; whether that is the closure of pre-existing cracks and pores during compaction or the opening of new cracks during dilatancy. By contrast, cumulative AE energy responds only to the growth of new, dilatant cracks. A full description of the experimental configuration can be found in Heap et al. (2009a). The values of applied stress in our study were also corrected for the increase in sample cross-sectional area during deformation.

A series of constant strain rate experiments were first performed at a strain rate of 1.0×10^{-5} s^{-1} under effective confining pressures (calculated as the confining pressure minus the pore fluid pressure, henceforth termed 'Peff') of 10, 30 and 50 MPa (obtained by applying confining pressures (Pc) of 30, 50 and 70 MPa with a constant pore fluid pressure (Pp) of 20 MPa), in order to ascertain the short-term peak stress (σ_p) and how it varies with Peff. This is necessary because σ_p is later used to guide the level of differential stress (Q) to be applied in constant stress (creep) experiments. Subsequently, conventional brittle creep experiments were conducted at constant, pre-determined values of Q that were fixed percentages of σ_p (see Baud and Meredith, 1997; Heap et al., 2009a, 2009b). Samples were first loaded to the pre-determined Q at a constant stressing rate of 5 MPa/min. The loading was then stopped, and the samples allowed to deform under constant Q (held constant using a servo-controlled pressure intensifier) until failure occurred after an extended period of time. It is important to perform such conventional creep experiments in order to ascertain if EB exhibits the classical type of trimodal creep behavior observed in other, primarily quartz-rich, rocks (Baud and Meredith, 1997; Heap et al., 2009a, 2009b; Lockner and Byerlee, 1977; Ngwenya et al., 2001; Tsai et al., 2008; Yang and Jiang, 2010). The experimental protocol is illustrated in Fig. 1, for an experiment performed under a Peff of 30 MPa and pre-loaded to 84% of σ_p (329 MPa) prior to creep. The

inset in Fig. 1 shows a plot of axial strain against time for the creep phase of the experiment. It clearly exhibits the type of trimodal behavior that has previously been shown to characterize brittle creep, and in particular an apparently constant strain rate during the extended phase of secondary creep.

While the type of conventional creep experiment described above provides high quality data, they commonly take a long time and provide only a single value of constant strain rate during secondary creep. However, previous work on creep in porous sandstones has demonstrated that it is possible to obtain multiple creep strain rates from a compound, stress-stepping creep experiment on a single sample, and thus improve experimental efficiency. In these experiments, stress steps, usually in the range 5 to 7 MPa, were imposed after the sample had undergone approximately 0.015–0.05 mm of axial shortening (equivalent to 0.015–0.05% axial strain) during secondary creep (for full details of the experimental procedure, see Heap et al., 2009a).

We therefore performed conventional creep experiments to ascertain if EB exhibits classic creep behavior over the whole range of applied pressure and stress conditions, and to investigate the influence of Q on time-to-failure. We subsequently ran stress-stepping creep experiments to investigate the influence of Q and Peff on creep strain rates. We report the results of these experiments in the following section.

4. Results

4.1. Constant strain rate experiments

Results from the constant strain rate experiments at different values of Peff are shown in Fig. 2. In each case, the stress–strain curves (Fig. 2a) exhibit the typical shape for rock deformed under triaxial compression. An initial hardening phase is followed by a pseudo-elastic phase and then a roll-over to the peak stress (σ_p). Peak stress is followed by a short phase of strain softening that leads to dynamic failure, marked by a rapid stress drop and formation of a shear fault.
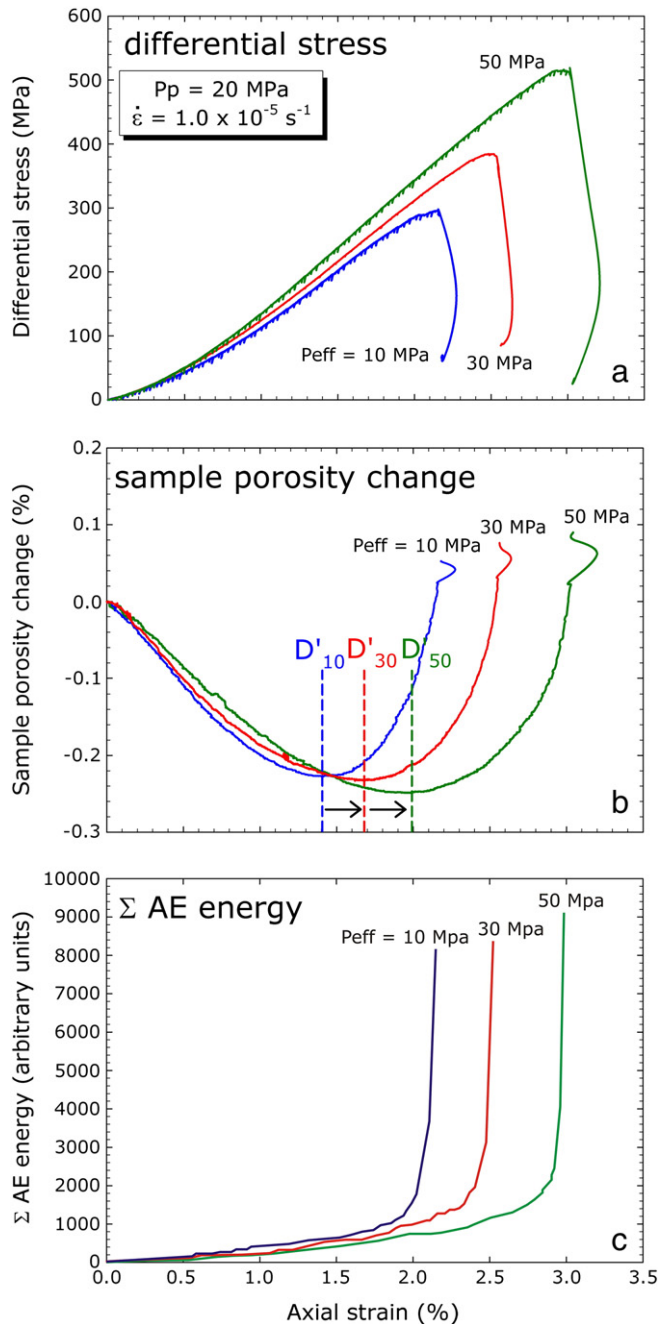
Fig. 2. Results from three triaxial compression experiments on EB conducted at constant strain rate but different effective confining pressures. Changes in the three proxies for crack damage within the rock are shown: (a) axial strain, (b) porosity change and (c) cumulative AE energy output (the area under each waveform). Experimental conditions are indicated on the figure. D′ marks the onset of dilatancy dominance. Peff—effective confining pressure; Pp—pore fluid pressure.

The data also show that increasing Peff results in significant increases in both σ_p and the axial strain at dynamic failure. The experiments yielded σ_p values of 291, 387 and 504 MPa at values of Peff of 10, 30 and 50 MPa, respectively. This is consistent with results reported in Benson et al. (2007) which gave a σ_p value of 475 MPa for water saturated EB at a Peff of 40 MPa.

The porosity change curves (Fig. 2b) show that sample deformation is initially dominated by compaction (porosity reduction due to closure of pre-existing cracks and pores) with dilatancy (porosity increase due to opening of new cracks) becoming more important in the later stages of deformation. The onsets of dilatancy dominance

(i.e. the points where dilatant crack opening exceeds compactive crack closure), that correspond to the minima in the porosity change curves, are marked as D′ for each value of Peff on Fig. 2b. Interestingly, not only does the position of D′ migrate to higher axial strain with increasing Peff (like σ_p), but the stress at which it occurs also remains an essentially constant proportion of σ_p ($63 \pm 2\%$). Whilst we would expect time-dependent brittle creep to occur at any stress level above that for the onset of dilatancy, our previous experience (Heap et al., 2009a, 2009b) has demonstrated that D′ marks the practical lower limit for studying brittle creep over realistic time scales in laboratory experiments. We therefore conducted all our creep experiments at values of Q at or beyond that equivalent to this point.

These observations are also reflected in the AE data shown in Fig. 2c. The AE energy rate is very low during the compactive phase of deformation and starts to increase as dilatant cracking becomes dominant. There is then a dramatic acceleration during the rollover to peak stress that continues right up to the point of dynamic failure. This has previously been interpreted as due to the coalescence of dilatant microcracks to form the macroscopic shear fault (e.g. see Benson et al., 2007). Our AE energy rate data are entirely consistent with that interpretation.

4.2. Conventional brittle creep experiments

Plots of axial strain against time for different values of constant Q are shown in Fig. 3a to d. All curves exhibit the type of trimodal behavior that characterizes brittle creep deformation. In all cases, the deformation is characterized by an initial phase of decreasing strain rate (primary creep), followed by an extended phase of apparently constant strain rate (secondary creep) and finally by a phase of accelerating strain rate (tertiary creep) that leads to localized shear failure (see Section 4.2 for details).

In order to ascertain if the strain rate during secondary creep was indeed constant we plotted the first derivatives of the strain-time curves (i.e. strain rates against time). An example of one such plot is shown in Fig. 4, and demonstrates that there is indeed an extended period of constant strain rate between the decelerating and accelerating creep phases. The creep strain rates during secondary creep (hereinafter simply referred to as the 'creep strain rate') were subsequently calculated from these constant strain rate portions of the creep curves and are given on Fig. 3. At this point we note that, while secondary creep proceeds at constant strain rate, it is not strictly a 'steady-state' process as has previously been claimed by many previous authors (e.g. Ngwenya et al., 2001; Yang and Jiang, 2010). Instead, it is clear from both the porosity change (Fig. 3e to h) and acoustic emission (Fig. 3i to l) curves that the state of damage in our samples is increasing systematically throughout the secondary creep phase.

The strain-time curves indicate that small changes in Q resulted in very large changes in both the creep strain rates and the times-to-failure (listed in Table 2). For example, for a Q of 375 MPa (97% of σ_p) the time-to-failure was close to 4 min and the calculated creep strain rate was $2.7 \times 10^{-6} \text{ s}^{-1}$. Reducing Q by only a small amount to 357 MPa (92% of σ_p) resulted in an increase in the time-to-failure to about 25 min and a decrease in strain rate to $4.1 \times 10^{-7} \text{ s}^{-1}$. Further reducing Q to 329 (85% of σ_p) and 304 MPa (79% of σ_p) altered the times-to-failure and strain rates to 270 and 4400 min and 4.0×10^{-8} and $2.4 \times 10^{-9} \text{ s}^{-1}$, respectively (Fig. 3a–d). In summary, reducing Q by a little under 20% resulted in an increase in time-to-failure and a decrease in creep strain rate of close to three orders of magnitude.

Porosity change and cumulative AE energy, used as proxies for accumulating damage within the sample, also exhibit trimodal behavior in all cases (Fig. 3e–l). However, we note that for the pore volume change curve at the lowest applied stress (Q=304 MPa; Fig. 2h) there is a much greater contribution to the total porosity change during the primary creep phase than for the experiments at
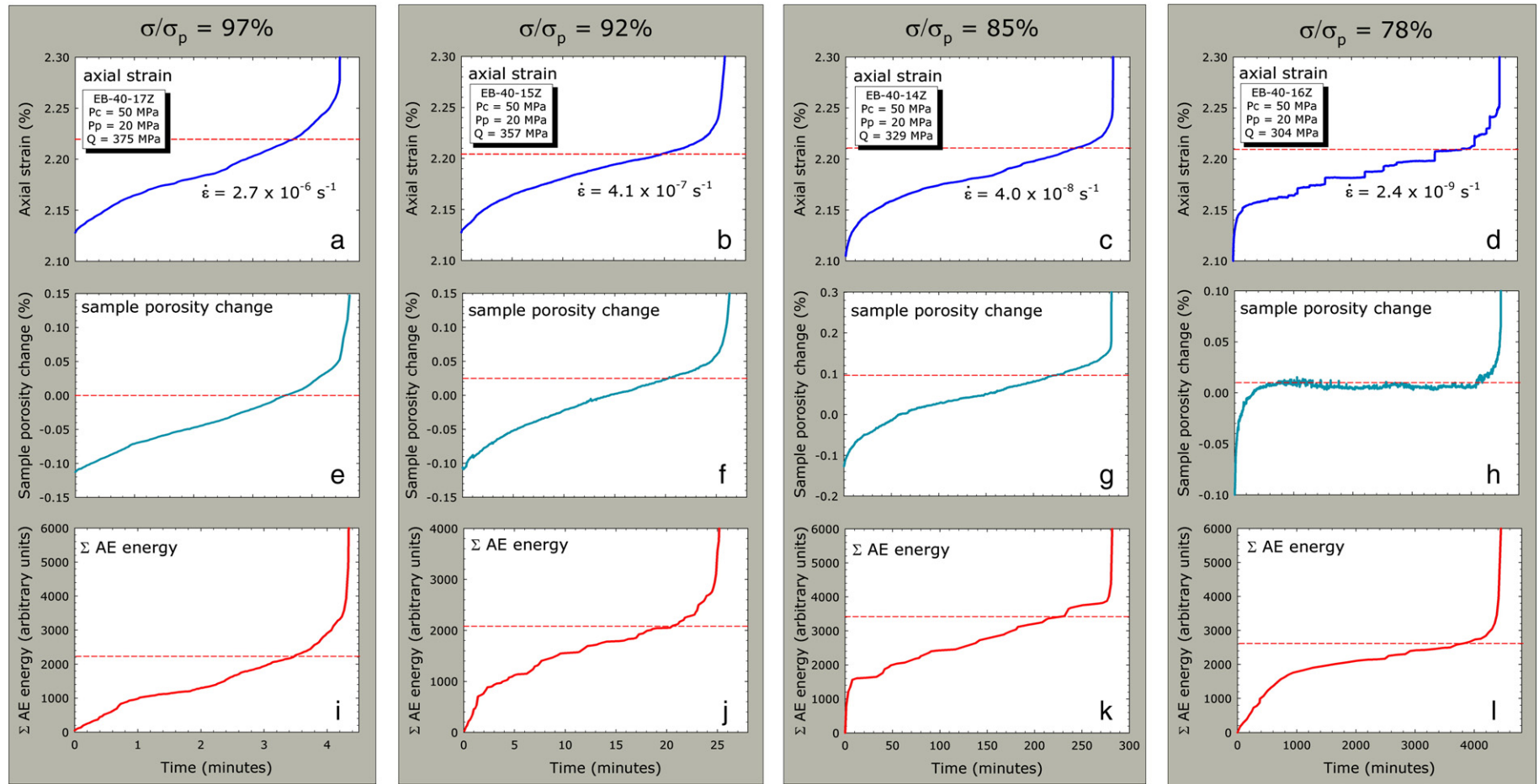
Fig. 3. Plots of the three damage proxies against time for four conventional brittle creep experiments on EB that have yielded creep strain rates over three orders of magnitude; (a)–(d), time–strain (creep) curves; (e)–(h), porosity change–time curves; and (k)–(l), ΣAE energy (the cumulative area under each waveform) time curves. The onset of accelerating tertiary creep is indicated in each figure by a dashed horizontal line. Experimental conditions are indicated on the figures. Pc—confining pressure; Pp—pore fluid pressure; Q—applied differential stress.
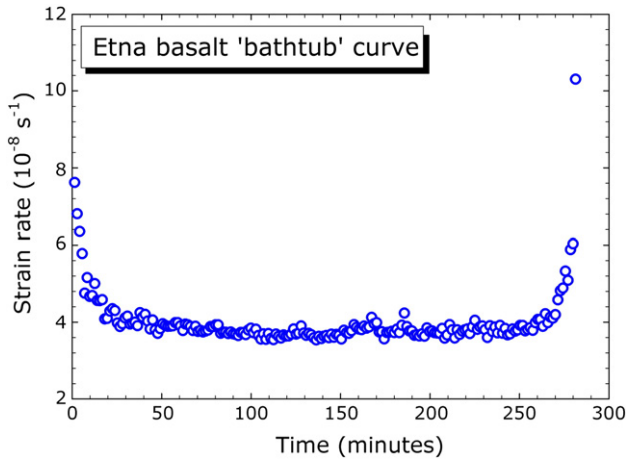
Fig. 4. Plot of strain rate against time (so-called "bathtub" plot) for conventional creep experiment EB-40-14Z run at a Q of 329 MPa (85% of σ_P). The curve shows an extended period between decelerating and accelerating creep that yielded a constant secondary creep strain rate of 4.0×10^{-8} s^{-1}.

higher Q. In fact, the porosity appears to remain essentially constant during the whole of the secondary creep phase. In all cases, the tertiary creep phase is characterized by accelerations in all three damage proxies (the onset of tertiary creep phase is marked by dashed horizontal lines in Fig. 3).

4.3. Stress-stepping brittle creep experiments

The influence of Q on creep strain rates was also investigated via stress-stepping experiments at a Peff of 30 MPa. Samples were first loaded to D′ at a constant stressing rate of 5 MPa/min, as shown in Fig. 1. The loading was then stopped and samples allowed to deform under a constant Q until they had undergone approximately 15–50 μm of axial shortening (equivalent to 0.015–0.05% axial strain). Following this, Q was increased by a small increment (5 to 7 MPa, equivalent to 2 to 3% of σ_p) and the process repeated until the sample eventually failed after a number of phases of creep. This method allowed creep strain rate data in the range 10^{-9} to 10^{-6} s^{-1} to be determined over 5 or 6 creep increments.

The relation between creep strain rate and differential stress (from both conventional and stress-stepping creep experiments) and time-to-failure and differential stress (from conventional creep experiments) are plotted on semi-log axes in Fig. 5a and b, respectively. Analysis of the experimental results show that creep strain rates can be described equally well by either a power law or exponential relation: strain rate = $(8.97 \times 10^{-8})Q^{32}$ or strain rate = $(1.84 \times 10^{-18})e^{0.1Q}$, and time-to-failure by either: time-to-failure = $1.7Q^{-32}$ or time-to-failure = $4.59e^{-0.1Q}$ (see Fig. 5). However, since both relations fit equally well, we cannot discriminate between them over the range of data achieved in our experiments; a problem previously noted in Bonnet et al. (2001). Our

Table 2
Experimental conditions, resultant creep strain rates and times-to-failure for the four reported conventional brittle creep experiments in Fig. 3.

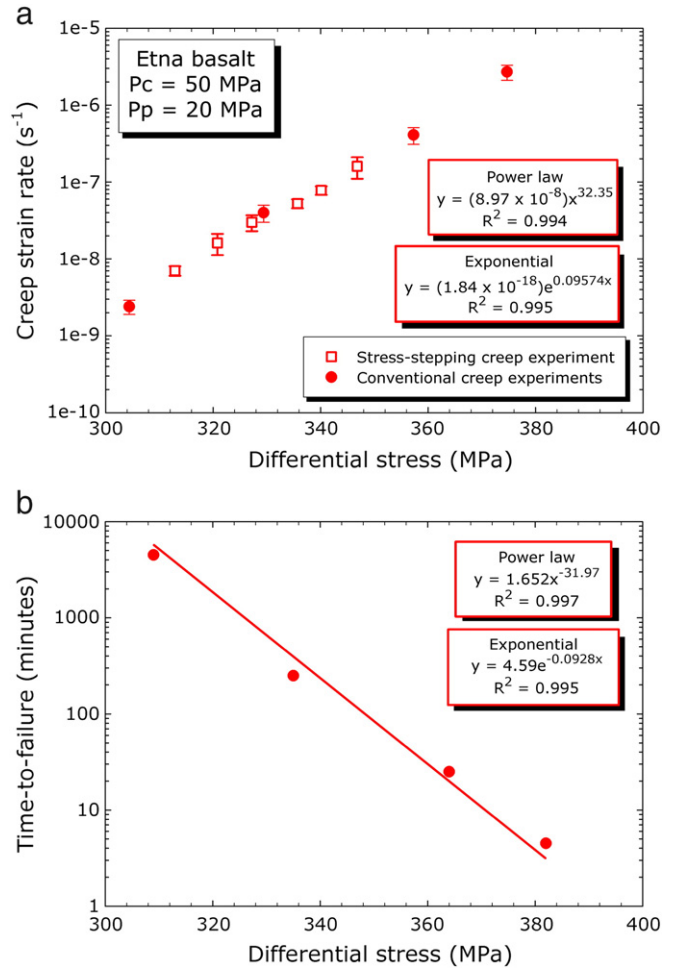| Sample	Applied creep stress (MPa)	Applied creep stress (% of σ_p)	Resultant creep strain rate (s^{-1})	Time-to-failure (min)
EB-40-16Z	304	78	2.4×10^{-9}	4400
EB-40-14Z	329	85	4.0×10^{-8}	270
EB-40-15Z	357	92	4.1×10^{-7}	25
EB-40-17Z	375	97	2.7×10^{-6}	4.5

Fig. 5. (a) Semi-log plot of creep strain rate against differential stress (Q) from both conventional creep experiments (filled circles) and stress-stepping creep experiments (hollow squares). (b) Semi-log plot of time-to-failure against differential stress for the four conventional creep experiments shown in Fig. 3. Experimental conditions are displayed on the figures. Pc—confining pressure; Pp—pore fluid pressure. The power law and exponential law fits to the experimental data are given on the figure. (For interpretation of the references to color in this figure legend, the reader is referred to the web version of this article.)

data also show that the strain rates measured in stress-stepping creep experiments are entirely consistent with those from conventional creep experiments (Fig. 3) under the same conditions.

Since stress-stepping is more experimentally efficient (as discussed above), we have used this technique to investigate the effect of varying the effective confining pressure on creep strain rates. Stress-stepping experiments were run at Peff values of 10, 30 and 50 MPa (whilst maintaining a constant Pp of 20 MPa). The results are presented in Fig. 6, again plotted on semi-log axes. The results illustrate the sensitivity of brittle creep to even modest changes in Peff. As Peff is increased, creep strain rates are shifted to much lower values for the same level of Q. This observation is entirely consistent with the results from our constant strain rate experiments (Fig. 2) which showed that the strength of EB increased significantly with increasing Peff. However, the increase in strength seen in the constant strain rate experiments as Peff was increased from 10 to 50 MPa was only about 75%, while Fig. 6 shows that the decrease in creep strain rate over the same Peff interval is multiple orders of magnitude. Furthermore, the gradients of the lines in Fig. 6, describing the relation between creep strain rate and Q, also decrease significantly as Peff is increased. Again, the data can be described equally well by either a
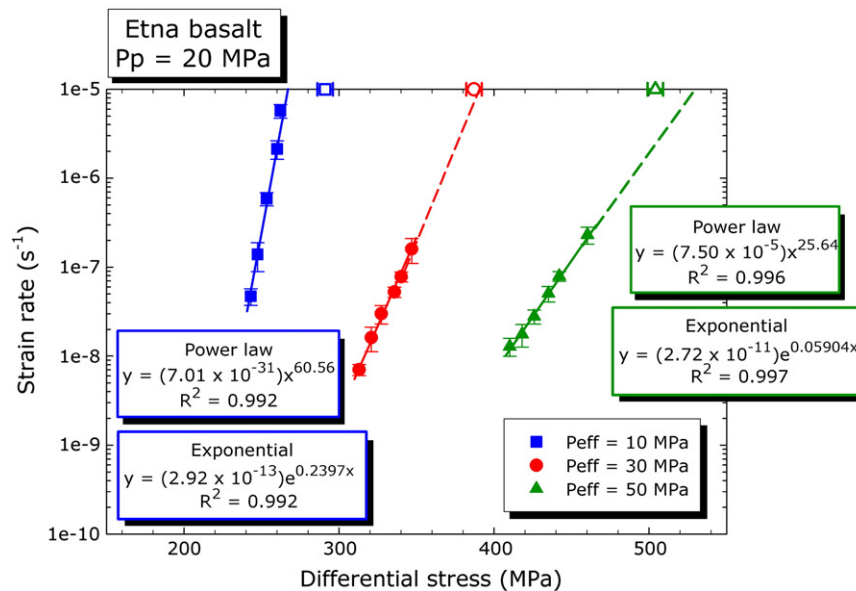
Fig. 6. Semi-log plot of creep strain rate data from stress-stepping experiments performed at effective confining pressures of 10 (solid squares), 30 (solid circles) and 50 MPa (solid triangles). Peak stress data from constant strain rate experiments (Fig. 2) are also plotted as open symbols at the appropriate strain rate. Experimental conditions are displayed on the figure. The power law and exponential law fits to the experimental data (for 10 and 50 MPa only, the fits for the 30 MPa data are shown on Fig. 5a) are given on the figure.

power or exponential law, with the governing equations and R^2 values given on Fig. 6.

4.4. Microstructural observations

We performed an additional conventional creep experiment in order to investigate the level of microcracking during secondary creep. In this experiment, a sample of EB was allowed to deform under a Q of 316 MPa until a significant proportion of secondary creep had elapsed, with care taken to ensure that the deformation was stopped prior to the onset of accelerating tertiary creep. After the desired amount of deformation had been achieved, the sample was carefully unloaded and removed from the apparatus. It was then impregnated with epoxy resin and cut in order to obtain thin sections for microstructural imaging using a field-emission scanning electron microscope (FESEM). For comparison, similar thin sections were prepared from (1) undeformed material and (2) a sample that had been taken to failure after tertiary creep under the same value of Q. Photo-micrographs from all three samples are shown in Fig. 7.

Fig. 7a, b and c shows photomicrographs of the undeformed material. The microcracks seen in the images illustrate the pervasive nature of the pre-existing microcrack damage in the EB used in this study, just as reported in previous studies on the same material (Benson et al., 2006; Fortin et al., 2011; Vinciguerra et al., 2005). Long, low aspect ratio microcracks are observed to have propagated thorough both the fine-grained matrix and larger crystals (Fig. 7a and c). In particular, many olivine phenocrysts are highly fractured (Fig. 7b).

Fig. 7d shows a composite photomicrograph of the sample from the experiment that was stopped after a significant proportion of secondary creep (as shown in the inset Fig. 7e). Here, a significant proportion of the pre-existing microcracks have propagated and started to coalesce into longer cracks. However, we consider that the majority of this deformation is more likely to have occurred during the >2% axial strain imposed on the sample during the constant stress rate loading to reach the 316 MPa creep stress than during the 0.02% axial strain accumulated during the creeping portion of the experiment.

Photomicrographs from the sample taken to failure after tertiary creep are shown in Fig. 7f, g and h. Fig. 7f shows a section of the

macroscopic shear fault that traversed the sample during failure (also shown in full in Fig. 7i), and Fig. 7g and h shows zoomed-in images from that section. We observe that the majority of the deformation is localized, with deformation-induced microcracking only found adjacent to the macroscopic fault plane. Indeed, Fig. 7h shows that only a few millimeters from the fault the microstructure appears essentially the same as that of the undeformed material.

While these observations are helpful in gaining a qualitative understanding of how the deformation progresses, we are forced to conclude that, taken together: (1) the pervasive network of pre-existing microcracks, (2) the small proportion of the total strain that is accumulated during creep relative to the initial, constant stress rate loading, and (3) the localized nature of the deformation during tertiary creep to failure, all militate against a unique quantitative interpretation of these microstructures. Similarly, Fortin et al. (2011) systematically measured the crack density of undeformed and failed samples of EB before and after constant strain rate deformation experiments. They found no significant variation in crack density between the different samples, but some indication of an increase in crack alignment in the deformed (failed) samples, in agreement with our observations reported above.

5. Discussion

5.1. Creep strain rates, damage levels and the influence of effective confining pressure

In this study, we have shown that water saturated basalt from Mt. Etna volcano exhibits trimodal brittle creep behavior when held under a constant Q that is a high proportion of σ_p. Both creep strain rates (Figs. 5a and 6) and times-to-failure (Fig. 5b) are shown to be strongly dependent on the level of Q (and can be equally well described by either a power or an exponential law), as previously observed for brittle creep in sandstones (Baud and Meredith, 1997; Heap et al., 2009a, 2009b; Ngwenya et al., 2001).

We note from our conventional creep data that the value of total axial strain at the onset of tertiary creep (marked by dashed horizontal lines on Fig. 3) is essentially the same ($2.21 \pm 0.01\%$) regardless of Q and the three orders of magnitude difference in the length of time required
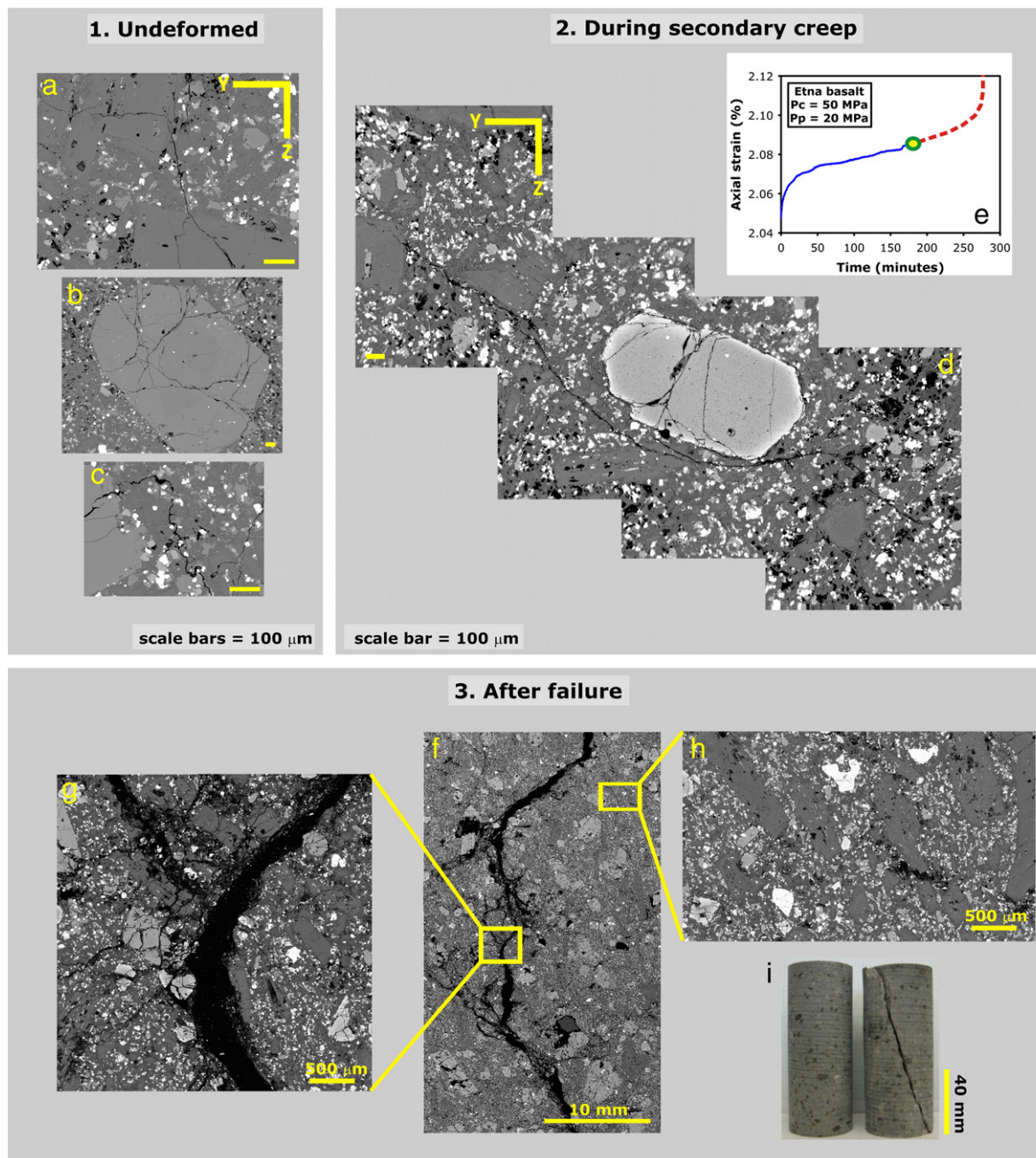
Fig. 7. FESEM photomicrographs of thin sections of EB taken: (1) in the undeformed state, (2) after a significant amount of secondary creep, and (3) after macroscopic failure. Inset in (2) shows the strain–time curve for the experiment, with the filled circle indicating the point at which the experiment was stopped and the dashed line indicating the projected path to failure. Inset in (3) shows the failed sample and an undeformed sample for comparison.

to reach this point (from 4 min to over 4000 min). This is true, even though 96% of the total strain is accumulated during the initial constant stress rate loading and only 4% during the creep deformation. Similarly, we also note that all three proxy measures of damage (axial strain, porosity change and cumulative AE energy) accumulate very similar values during primary and secondary creep (again marked by dashed horizontal lines in Fig. 3); axial strain of $0.10 \pm 0.02\%$, porosity change of 0.15 ± 0.05 and cumulative AE of 2400 ± 300 units. Taken together, these observations suggest that a critical level of damage is required to initiate the onset of acceleration to failure (tertiary creep). This is consistent with observations of the same phenomenon in previous experimental studies of brittle creep in other rocks (Baud and Meredith, 1997; Heap et al., 2009a, 2009b; Kranz and Scholz, 1977).

Results from stress-stepping creep experiments have illustrated that even a modest increase in Peff result in very large decreases in creep strain rates, for any given Q. These decreases can only be partially explained by the known increase in strength (σ_p) with increase in Peff as shown in Fig. 2. At Peff values of 10, 30 and 50 MPa, the σ_p values were 291, 387 and 504 MPa respectively, and these values have been added to Fig. 6 (open symbols) at the appropriate strain rate of $10^{-5} s^{-1}$ for comparison. Fig. 6 shows that, while substantial changes in creep strain rate can be attributed to the purely mechanical influence of changing Peff (e.g. the inhibition of tensile crack growth); this can by no means explain all of the observed changes. We see that the shift along the differential stress axis is greater for the creep data than for the constant strain rate data. Similar

to Heap et al. (2009a), we suggest that the larger than expected changes in strain rate are due to changes in the rate of water–rock chemical reactions at the different effective pressures. Any decrease in crack aperture at higher Peff will inhibit the transport of reactive species to the crack tips, thus inhibiting the rate of stress corrosion cracking. Conversely, any increase in crack aperture at lower Peff will enhance transport and thus enhance the rate of cracking. These observations are consistent with previously published observations of creep in granite and sandstone (Kranz, 1980; Ngwenya et al., 2001).

Also evident in Fig. 6 is that the creep strain rate–Q curves show a decrease in gradient as Peff is increased. The reason for this decrease is not clear, but is likely to result from a combined chemical and mechanical effect. Further investigation would require comparative measurements on both dry and saturated samples over the same range of Q and strain rate. We note, however, that very similar changes in the gradients of creep strain rate–Q curves were seen during brittle creep of sandstone, as reported by Heap et al. (2009a).

5.2. Macroscopic creep law

Macroscopic creep laws are necessary if we wish to extrapolate our laboratory data in an attempt to understand the process of brittle creep in rocks at the time-scales and strain rates that are typical of large scale deformation in the crust. Recently, Heap et al. (2009a) demonstrated that the mean-field damage mechanics model of Main (2000) was able to reproduce the strain–time curves from their creep experiments on sandstone. This model invokes a two stage process: (1) strain hardening that involves distributed crack damage, and (2) strain softening that involves crack interaction and coalescence. The strain rate associated with process (1) is expected to decrease as a power-law function of time, and hence this signal will dominate in the early stage of deformation. The strain rate associated with process (2) is expected to accelerate as a power-law function of time and hence dominate in the later stage of deformation. In this scenario, secondary (constant strain rate) creep emerges simply as an extended balance between these two competing processes. The evolution of total strain (Ω) with time, for instantaneous loading to the creep stress, is consequently a sum of these two accelerating and decelerating power-law rate functions and shown by Main (2000) to be:

$$\Omega(t) = \Omega_I (1 + t/T)^m + \Omega_{III}\left(1 - t/t_f\right)^{-v}, \qquad (1)$$

where the amplitudes Ω_I and Ω_{III} represent primary and tertiary creep components respectively, T is the characteristic transient timescale associated with primary creep, t_f is the asymptotic failure time and m and v are positive power law exponents.

Rigorous statistical fitting of such a two-component power-law model with six parameters to experimental creep strain data is a challenging problem in non-linear statistical inference and beyond the scope of the current paper. Additionally, the model requires further development in order to accommodate the finite time of loading to the creep stress at constant stress rate in our experiments, and this is the subject of current work. Here, therefore, we fit a single power-law model to the final one third of the strain data from each of our four conventional creep experiments (Fig. 3), since this encompasses all of the accelerating (tertiary) phase, where process (2), strain softening, is expected to dominate. For these phases of the experiments, the evolution of strain rate with time is expected to be approximated by:

$$d\Omega/dt = k\left(1 - t/t_f\right)^{-p}, \qquad (2)$$

where k is the strain rate at $t = 0$ and $p = 1 + v$. We apply a maximum likelihood fit, using a generalized linear regression model to the strain rate data, assuming a Gaussian error structure. The maximum-

likelihood fit minimizes bias in the inversion. The fit to strain rate, instead of fitting the model to total or cumulative strain, is consistent with the assumptions of independent or uncorrelated data inherent in the regression technique (Greenhough et al., 2009). Gaussian error structure is a priori consistent with the qualitative pattern of the scatter on the data in Fig. 5. We define the failure time (t_f) as the time of maximum strain rate.

Power law plots of strain rate as a function of time before failure ($t_f - t$) from the maximum-likelihood model (with 95% confidence limits) are shown in Fig. 8, together with the experimental data (solid symbols). The distribution of data points about the model fits is, *a posteriori*, generally consistent with assumption of a Gaussian error structure. Overall, there is no evidence for any strain rate dependence of the tertiary creep exponent, implying a single underlying process that is independent of strain rate within the three orders of magnitude studied here. More remarkably, the exponent $p = 1 + v$ has a mean value of close to 1.0 ± 0.3. This value is consistent with accelerating power-law exponents observed in analogous natural systems such as tectonic seismicity rates (e.g. Bufe and Varnes, 1993; Hainzl et al., 1999) and seismicity and strain rates before volcanic eruptions (e.g. Kilburn and Voight, 1998; Voight, 1988). This apparent universality is remarkable, given the range of spatial and temporal scales involved. Regional tectonic strain rates in active zones are on the order of $10^{-15}\,\mathrm{s}^{-1}$ (Ekström and England, 1989; Whitten, 1956; Wood, 1973), compared to $10^{-8}\,\mathrm{s}^{-1}$ for the slowest of our laboratory tests, and occur on scales of hundreds of km rather than a few cm. This implies a universality of scaling across 7 orders of magnitude in both space and time.

Apart from their intrinsic interest, volcano-tectonic settings are useful in examining scaling relations for constitutive rules of brittle-field rock deformation because the strain rates are higher, and involve a less dramatic extrapolation from laboratory rates. Although highly variable, typical deformation rates at volcanic edifices are on the order of $10^{-11}\,\mathrm{s}^{-1}$ and faster (see Takada, 1994 and references therein) on objects a few km in diameter, i.e. only three orders of magnitude in time and five in space compared with the slowest laboratory tests presented here.

5.3. Is brittle creep an important process at active basaltic volcanoes?

Our experimental results have shown that basalt undergoes brittle creep at pressures and strain rates expected to exist within volcanic edifices. Further, this combination of material and environment appears ideal for the occurrence of geologically fast rates of stress corrosion cracking. Firstly, edifice-forming basaltic rocks commonly contain a high density of pre-existing crack damage (e.g. see Heap
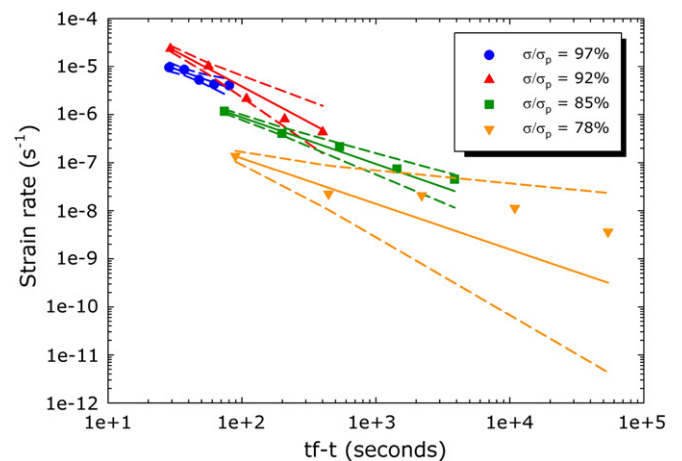

Fig. 8. Maximum-likelihood power-law fits to the accelerating phases of strain for the conventional creep experiments shown in Fig. 3, together with their 95% confidence limits.

et al., 2009c; Vinciguerra et al., 2005), providing both multiple stress concentration sites for the nucleation of crack growth and multiple pathways for fluid transport to crack tips. Secondly, and somewhat related to the first point, the rocks are also commonly porous and highly permeable (Vinciguerra et al., 2005). For this reason volcanic edifices commonly host large reservoirs of water, an essential prerequisite for stress corrosion cracking. Finally, although the influence of temperature on time-dependent brittle creep in basalt was not specifically addressed in this study, it is well-known that stress corrosion reactions are significantly enhanced at elevated temperatures, as would be the case with circulating magmatic fluids (Driesner and Geiger, 2007; Meredith and Atkinson, 1985; Michalske and Bunker, 1987; Michalske and Freiman, 1982; Waza et al., 1980).

Seismic activity and subsequent strain release recorded between 1993 and 2005 at Mt. Etna volcano are presented in Fig. 9 (after Allard et al., 2006) and are seen to display temporal characteristics comparable with the phases of primary, secondary and tertiary creep observed in our laboratory experiments (Fig. 3). Strain release is seen to accelerate prior to either dyke intrusion (January 1998) or eruption (July 2001). Afterwards, the strain release decelerates before reaching a steady rate. This brittle deformation, interpreted as due to a step increase in stress caused by magma intrusion (Palano et al., 2009), consists of ground deformation of the order of tens of centimeters and the occurrence of swarms of thousands of earthquakes, with magnitudes up to 4.5. After a period of time, strain release accelerates again and another dyke intrusion/eruption occurs. Although this volcanic example involves only the seismic component of strain (and does not therefore take into account aseismic creep on faults, and aseismic dike opening, e.g. Baer and Hamiel, 2010; Baer et al., 2008; Grandin et al., 2009; Wright et al., 2006), we believe it is indicative of the wider pattern of deformation. Firstly, Voight (1988) showed that both strain rate and energy release rate before volcanic eruptions can be observed to follow similar accelerating trends. Secondly, our experiments show that strain-rate and seismic AE rate follow very similar trends (Fig. 3).

The lava piles at Mt. Etna are pervasively fractured at all scales. While meso- and macroscopic faults are usually very important for driving large-scale deformation, combined GPS and radar interferometry (InSAR) measurements at Mt. Etna indicate that deformation is not restricted to large fault systems (e.g. see Palano et al., 2008); nor do they identify a large décollement surface. This suggests that the large-scale deformation must be, to some degree, accommodated by the time-dependent deformation of the edifice-forming rocks, rather than the simple reactivation of pre-existing faults or fractures. We also note that it is now well-established that fracturing is a scale-invariant process across many orders of magnitude. Fracture scaling, using the well-known size-frequency scaling relation of Aki and Richards (2002) has previously been applied successfully to laboratory AE and fracture data on basalt under a range of experimental conditions. For example, Burlini et al. (2007) applied this technique to high temperature fracture and dyke penetration, and Benson et al. (2008) applied it to long-period seismicity associated with rapid fluid flow in fractures, over 5 orders of magnitude. It should not be surprising that creep laws obtained in the laboratory scale directly to volcano settings (e.g. Voight, 1988) since, stress corrosion constitutive laws for the microscopic process, rheological laws for the mesoscopic behavior of bulk rock, and a simple fracture percolation law near the macroscopic percolation threshold (which accounts in the simplest way for structural and material heterogeneity), are all consistent with power-law acceleration to failure (Main, 1999). This implies that the constitutive laws reflect the statistical physics of sub-critical processes rather than solely the underlying cause. They would therefore be expected to have the same constitutive laws (exponential or inverse power law acceleration) albeit with different exponents. Nevertheless, stress corrosion is an important known microscopic process in rock deformation, and is enabled by the high pore pressures, high temperatures, and low loading rates expected within a volcanic edifice. The material strengths obtained in our laboratory experiments would be an upper bound to the failure stresses for a much larger object such as a volcanic edifice which itself is subject to near critical constant or very slowly varying (i.e. 'creep') stresses due to a combination of high pore pressures (low normal stresses) and high slope angles (high shear stresses). We would therefore expect different processes to operate on different scales, and here we
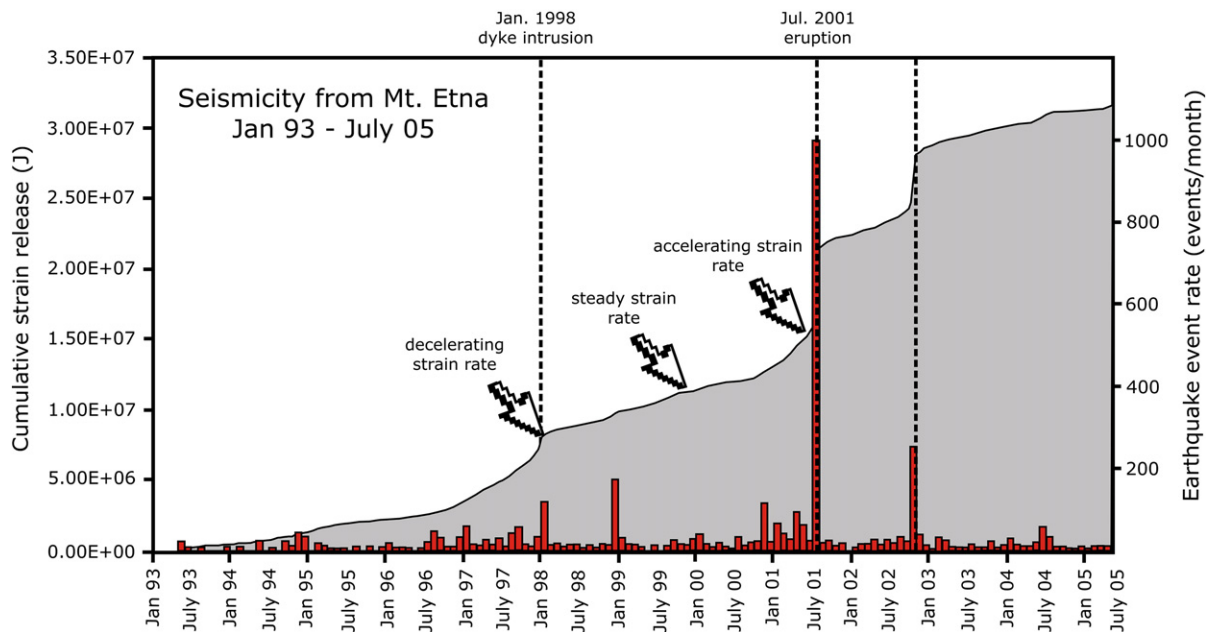

Fig. 9. Deformation at Mt. Etna volcano between January 1993 and July 2005 (after Allard et al., 2006). Seismic event rate is shown in red, and cumulative strain release is shown in gray. The January 1998 dyke intrusion and the July 2001 eruption are also indicated. Earthquake event rate is shown by the red bars, and cumulative strain release is shown by the shaded (gray) area. (For interpretation of the references to color in this figure legend, the reader is referred to the web version of this article.)

emphasize the microscopic one, while accepting that renormalization to larger scale is likely to involve changes in the distribution exponents.

However, we would urge caution in applying our laboratory deformation results directly to time-dependent deformation of volcanoes. In the laboratory we are able to control the stress, the confining pressure and the pore fluid pressure and chemistry precisely on a relatively homogeneous and isotropic sample. By contrast, all of these parameters, as well as temperature, are likely to be spatially heterogeneous within any large volcanic edifice. This means that the time-dependent material response to stress is likely to be much more complex in a volcano than that in a laboratory sample. Volcano deformation is more likely to comprise an aggregate of deformation on different heterogeneous elements, each undergoing brittle creep, but with different material properties and subject to local stress, temperature and pore fluid conditions. Nevertheless, the underlying process of time-dependent brittle creep is likely to be an important deformation mechanism operating in all stressed, basaltic volcanic edifices and therefore should be taken into account when assessing their deformation state and stability.

6. Conclusions

1. We have shown that a basalt from Mt. Etna undergoes time-dependent brittle creep when held at a Q that is a high proportion of σ_p. All three classic creep phases, primary (decelerating), secondary (steady-rate) and tertiary (accelerating), were observed.
2. Both creep strain rates and times-to-failure are shown to be highly dependent the level of Q (and can be equally well described by a power law or an exponential law).
3. We note from our conventional creep data that the values of damage at the onset of tertiary creep are essentially similar regardless of Q and the three orders of magnitude difference in the length of time required to reach this point (from 4 min to over 4000 min). These observations suggest that a critical level of damage is required to initiate the onset of acceleration to failure (tertiary creep).
4. Results from stress-stepping creep experiments have demonstrated that even modest increases in Peff result in very large decreases in creep strain rates, for any given Q. We suggest that only part of this change can be attributed to the purely mechanical influence of an increase in pressure, the remainder is interpreted as due to a reduction in stress corrosion reactions, a result of a reduction in crack aperture that restricts the rate of transport of reactive species to crack tips.
5. A generalized linear regression power-law model, fit to the final one third of the strain data from each of our four conventional creep experiments, suggests that there is no evidence for any strain rate dependence of the tertiary creep exponent, implying a single underlying process.
6. Seismic activity and subsequent strain release recorded between 1993 and 2005 at Mt. Etna volcano is seen to display temporal characteristics comparable with the phases of primary, secondary and tertiary creep observed in our laboratory experiments. We therefore propose that the underlying process of time-dependent brittle creep is likely to be an important deformation mechanism operating in all stressed, basaltic volcanic edifices.

Acknowledgements

References

Aki, K., Richards, P.G., 2002. Quantitative Seismology, second edition. University Science Books, Sausalito, California, USA0-935702-96-2.
Allard, P., Behncke, B., D'Amico, S., Neri, M., Gambino, S., 2006. Mount Etna 1993–2005: anatomy of an evolving eruptive cycle. Earth Sci. Rev. 78, 1–2.
Anderson, O.L., Grew, P.C., 1977. Stress corrosion theory of crack propagation with applications to geophysics. Rev. Geophys. 15, 77–104.
Andrade, E.N., Randall, R.F.Y., 1949. The Rehbinder effect. Nature 164, 1127.
Armitrano, D., Helmstetter, A., 2006. Brittle creep, damage, and time to failure in rocks. J. Geophys. Res. 111. doi:10.1029/2005JB004252.
Atkinson, B.K., 1984a. Subcritical crack growth in geological materials. J. Geophys. Res. 89, 4077–4114.
Atkinson, B.K., 1984b. Subcritical crack growth in geological materials. J. Geophys. Res. 89, 4077–4114.
Atkinson, B.K., Meredith, P.G., 1987. The theory of subcritical crack growth with applications to minerals and rocks. In: Atkinson, B.K. (Ed.), Fracture Mechanics of Rock. Academic Press, London, pp. 111–166.
Baer, G., Hamiel, G., 2010. Form and growth of an embryonic continental rift: InSAR observations and modelling of the 2009 western Arabia rifting episode. Geophys. J. Int. 182, 155–167.
Baer, G., Hamiel, Y., Shamir, G., Nof, R., 2008. Evolution of a magma-driven earthquake swarm and triggering of the nearby Oldoinyo Lengai eruption, as resolved by InSAR, ground observations and elastic modeling, East African Rift, 2007. Earth Planet. Sci. Lett. 272, 339–352.
Baud, P., Meredith, P.G., 1997. Damage accumulation during triaxial creep of Darley Dale sandstone from pore volumometry and acoustic emission. Int. J. Rock Mech. Min. Sci. 34 (3–4) Paper No. 024.
Benson, P.M., Schubnel, A., Vinciguerra, S., Trovato, C., Meredith, P.G., Young, R.P., 2006. Modeling the permeability evolution of microcracked rocks from elastic wave velocity inversion at elevated isostatic pressure. J. Geophys. Res. 111 (B04202). doi:10.1029/2005JB003710.
Benson, P.M., Thompson, B.D., Meredith, P.G., Vinciguerra, S., Young, R.P., 2007. Imaging slow failure in triaxially deformed Etna basalt using 3D acoustic-emission location and X-ray computed tomography. Geophys. Res. Lett. 34 (L03303). doi:10.1029/2006GL028721.
Benson, P.M., Vinciguerra, S., Meredith, P.G., Young, R.P., 2008. Laboratory simulation of volcano seismicity. Science 322, 249–252.
Bonaccorso, A., Calvari, S., Coltelli, M., Del Negro, C., Falsaperla, S., 2004. In: Bonaccorso, A., Calvari, S., Coltelli, M., Del Negro, C., Falsaperla, S. (Eds.), Mount Etna: Volcano Laboratory: Am. Geophys. Union Geophys. Monogr., 143.
Bonforte, A., Puglisi, G., 2003. Magma uprising and flank dynamics on Mt. Etna volcano, studied by GPS data (1994–1995). J. Geophys. Res. 108 (B3), 2153–2162.
Bonforte, A., Puglisi, G., 2006. Dynamics of the eastern flank of Mt. Etna volcano (Italy) investigated by a dense GPS network (2006). J. Volcanol. Geotherm. Res. 153, 357–369.
Bonnet, E., Bour, O., Odling, N.E., Davy, P., Main, I., Cowie, P., Berkowitz, B., 2001. Scaling of fracture systems in geological media. Rev. Geophys. 39, 347–383.
Borgia, A., Ferrari, L., Pasquare, G., 1992. Importance of gravitational spreading in the tectonic and volcanic evolution of Mount Etna. Nature 357, 231–235.
Borgia, A., Delaney, P.T., Denlinger, R.P., 2000. Spreading volcanoes. Annu. Rev. Earth Planet. Sci. 28, 539–570.
Bufe, C.G., Varnes, D.J., 1993. Predictive modeling of the seismic cycle of the greater San Francisco Bay region. J. Geophys. Res. 98 (B6), 9871–9883.
Burlini, L., Vinciguerra, S., Di Toro, G., De Natale, G., Meredith, P.G., Burg, J.-P., 2007. Seismicity preceding volcanic eruptions: new experimental insights. Geology 35, 183–186.
Charles, R.J., 1958. Static fatigue of glass. J. Appl. Phys. 29, 1549–1560.
Chastin, S.F.M., Main, I.G., 2003. Statistical analysis of daily seismic event rate as a precursor to volcanic eruptions. Geophys. Res. Lett. 30 (No. 13). doi:10.1029/2003GL016900.
Cornelius, R.R., Scott, P.A., 1993. A materials failure relation of accelerating creep as empirical description of damage accumulation. Rock Mech. Rock Eng. 26 (3), 233–252.
Costin, 1987. Time-dependent deformation and failure. In: Atkinson, B.K. (Ed.), Fracture Mechanics of Rock. Academic Press, London, pp. 167–216.
Driesner, T., Geiger, S., 2007. Numerical simulation of multiphase fluid flow in hydrothermal systems. Rev. Mineral. Geochem. 65, 187–212.
Ekström, G., England, P., 1989. Seismic strain rates in regions of distributed continental deformation. J. Geophys. Res. 94 (No. B8), 10231–10257.
Fortin, J., Stanchits, S., Vinciguerra, S., Guéguen, Y., 2011. Influence of thermal and mechanical cracks on permeability and elastic wave velocities in a basalt from Mt. Etna volcano subjected to elevated pressure. Tectonophysics 503, 60–72.
Freiman, S.W., 1984. Effects of the chemical environment on slow crack growth in glasses and ceramics. J. Geophys. Res. 89, 4072–4077.
Fujii, Y., Kiyama, T., Ishjima, Y., Kodama, J., 1999. Circumferential strain behaviour during creep tests of brittle rocks. Int. J. Rock Mech. Min. Sci. 36, 323–337.
Grandin, R., Socquet, A., Binet, R., Klinger, Y., Jacques, E., de Chabalier, J.-B., King, G.C.P., Lasserre, C., Tait, S., Tapponnier, P., Delorme, A., Pinzuti, P., 2009. September 2005

Manda Hararo–Dabbahu rifting event, Afar (Ethiopia): constraints provided by geodetic data. J. Geophys. Res. 114, B08404. doi:10.1029/2008JB005843.

Greenhough, J., Bell, A.F., Main, I.G., 2009. Comment on "Relationship between accelerating seismicity and quiescence, two precursors to large earthquakes" by Arnaud Mignan and Rita Di Giovambattista. Geophys. Res. Lett. 36. doi:10.1029/2009GL039846.

Hadizadeh, J., Law, R.D., 1991. Water-weakening of sandstone and quartzite deformed at various stress and strain rates. Int. J. Rock Mech. Min. Sci. Geomech. Abstr. 28, 431–439.

Hainzl, S., Zoeller, G., Kurths, J., 1999. Similar power laws for fore- and aftershock sequences in a spring-block model for earthquakes. J. Geophys. Res. 104 (B4), 7243–7253.

Hamiel, Y., Katz, O., Lyakhovsky, V., Reches, Z., Fialko, Y., 2006. Stable and unstable damage evolution in rocks with implications to fracturing granite. Geophys. J. Int. 167, 1005–1016.

Heap, M.J., Baud, P., Meredith, P.G., Bell, A.F., Main, I.G., 2009a. Time-dependent brittle creep in Darley Dale sandstone. J. Geophys. Res. 114, B07203. doi:10.1029/2008JB006212.

Heap, M.J., Baud, P., Meredith, P.G., 2009b. The influence of temperature on brittle creep in sandstones. Geophys. Res. Lett. doi:10.1029/2009GL03973

Heap, M.J., Vinciguerra, S., Meredith, P.G., 2009c. The evolution of elastic moduli with increasing crack damage during cyclic stressing of a basalt from Mt. Etna volcano. Tectonophysics 471, 153–160.

Hillig, W.B., Charles, R.J., 1965. Surfaces, stress-dependent reactions, and strength. In: Zackay, V.F. (Ed.), High Strength Materials. John Wiley and Sons, New York, pp. 682–705.

Jaeger, J., Cook, N.G.W., Zimmerman, R., 2007. Fundamentals in Rock Mechanics, 4th Edition. Blackwell Publishing, London.

Jeong, H.-S., Kang, S.-S., Obara, Y., 2007. Influence of surrounding environments and strain rates on the strength of rocks subjected to uniaxial compression. Int. J. Rock Mech. Min. Sci. 44, 321–331.

Katz, O., Reches, Z., 2004. Microfracturing, damage, and failure of brittle granites. J. Geophys. Res. 109, B01206. doi:10.1029/2002JB001961.

Kilburn, C.R.J., 2003. Multiscale fracturing as a key to forecasting volcanic eruptions. J. Volcanol. Geotherm. Res. 125, 271–289.

Kilburn, C.R.J., Voight, B., 1998. Slow rock fracture as eruption precursor at Soufriere Hills volcano, Montserrat. Geophys. Res. Lett. 25, 3665–3668.

Kranz, R., 1980. The effect of confining pressure and stress difference on static fatigue of granite. J. Geophys. Res. 85, 1854–1866.

Kranz, R., Scholz, C.H., 1977. Critical dilatant volume of rocks at the onset of tertiary creep. J. Geophys. Res. 82, 4893–4898.

Kranz, R., Harris, W.J., Carter, N.L., 1982. Static fatigue of granite at 200 °C. Geophys. Res. Lett. 9, 1–4.

Kurita, K., Swanson, P.L., Getting, I.C., Spetzler, H., 1983. Surface deformation of Westerly granite during creep. J. Geophys. Res. 10, 75–78.

Lawn, B., 1993. Fracture of Brittle Solids. Cambridge University Press, Cambridge.

Lockner, D., 1993. Room temperature creep in saturated granite. J. Geophys. Res. 98, 475–487.

Lockner, D., 1998. A generalized law for brittle deformation of Westerly granite. J. Geophys. Res. 103, 5107–5123.

Lockner, D., Byerlee, J., 1977. Acoustic emission and creep in rocks at high confining pressure and differential stress. Bull. Geol. Soc. Am. 67, 247–258.

Lockner, D.A., Byerlee, J.D., 1986. Changes in complex resistivity during creep in granite. Pageoph. 124 (Nos. 4/5), 659–676.

Main, I.G., 1999. Applicability of time-to-failure analysis to accelerated strain before earthquakes and volcanic eruptions. Geophys. J. Int. 139, F1–F6.

Main, I.G., 2000. A damage mechanics model for power-law creep and earthquake 556 aftershock and foreshock sequences. Geophys. J. Int. 142, 151–161.

Maranini, E., Yamaguchi, T., 2001. A non-associated viscoplastic model for the behaviour of granite in triaxial compression. Mech. Mater. 33, 283–293.

McGuire, W.J., Kilburn, C.R.J., 1997. Forecasting volcanic events: some contemporary issues. Geol. Rundsch. 86, 439–445.

Meredith, P.G., Atkinson, B.K., 1983. Stress corrosion and acoustic emission during tensile crack propagation in Whin Sill dolerite and other basic rocks. Geophys. J. Int. 75, 1–21.

Meredith, P.G., Atkinson, B.K., 1985. Fracture toughness and critical crack growth during high-temperature tensile deformation of Westerly granite and Black gabbro. Phys. Earth Planet. Inter. 39, 33–51.

Michalske, T.A., Bunker, B.C., 1987. Steric effects in stress corrosion fracture of glass. J. Am. Ceram. Soc. doi:10.1111/j.1151-2916.1987.tb04879.x

Michalske, T.A., Freiman, S.W., 1982. A molecular interpretation of stress corrosion in silica. Nature 295, 511–512.

Nara, Y., Kaneko, K., 2005. Study of subcritical crack growth in andesite using the Double Torsion test. Int. J. Rock Mech. Min. Sci. 42, 521–530.

Nara, Y., Takada, M., Mori, D., Owada, H., Yoneda, T., Kaneko, K., 2010. Subcritical crack growth and long-term strength in rock and cementitious material. Int. J. Fract. doi:10.1007/s10704-010-9455-z

Ngwenya, B.T., Main, I.G., Elphick, S.C., Crawford, B.R., Smart, B.G.D., 2001. A constitutive law for low-temperature creep of water-saturated sandstones. J. Geophys. Res. 106, 21811–21826.

Ogniben, L., 1966. Lineamenti idrogeologici dell'Etna. Riv. Min. Sic. 100–102, 1–24.

Orowan, E., 1944. The fatigue of glass under stress. Nature 154, 341–343.

Palano, M., Puglisi, G., Gresta, S., 2008. Ground deformation patterns at Mt. Etna from 1993 to 2000 from joint use of InSAR and GPS techniques. J. Volcanol. Geotherm. Res. 169, 99–120.

Palano, M., Gresta, S., Puglisi, G., 2009. Time-dependent deformation of the eastern flank of Mt. Etna: after-slip or viscoelastic relaxation? Tectonophysics 473, 300–311.

Rehbinder, P.A., 1948. Hardness Reducers in Drilling (translated from Russian). CSIR, Melbourne.

Rust, D., Behncke, B., Neri, M., Ciocanel, A., 2005. Nested zones of instability in the Mount Etna volcanic edifice, Sicily. J. Volcanol. Geotherm. Res. 144, 137–153.

Smith, R., Kilburn, C.R.J., 2010. Forecasting eruptions after long repose intervals from accelerating rates of rock fracture: the June 1991 eruption of Mount Pinatubo, Philippines. J. Volcanol. Geotherm. Res. 191, 129–136.

Stanchits, S., Vinciguerra, S., Dresen, G., 2006. Ultrasonic velocities, acoustic emission characteristics and crack damage of basalt and granite. Pure Appl. Geophys. 163, 974–993.

Swanson, P.L., 1984. Subcritical crack growth and other time- and environmental-dependent behaviour in crustal rocks. J. Geophys. Res. 89, 4137–4152.

Takada, A., 1994. The influence of regional stress and magmatic input on styles of monogenetic and polygenetic volcanism. J. Volcanol. Geotherm. Res. 99, 13563–13573.

Tanguy, J.C., Condomines, M., Kieffer, G., 1997. Evolution of the Mount Etna magma: constraints on the present feeding system and eruptive mechanism. J. Volcanol. Geotherm. Res. 75, 221–250.

Terzaghi, K., 1943. Theoretical Soil Mechanics. John Wiley and Sons, New York.

Tsai, L.S., Hsieh, Y.M., Weng, M.C., Huang, T.H., Jeng, F.S., 2008. Time-dependent deformation behaviors of weak sandstones. Int. J. Rock Mech. Min. Sci. 45, 144–154.

Vinciguerra, S., Trovato, C., Meredith, P.G., Benson, P.M., 2005. Relating seismic velocities, thermal cracking and permeability in Mt. Etna and Iceland basalts. Int. J. Rock Mech. Min. Sci. 42, 900–910.

Voight, B., 1988. A method for prediction of volcanic eruptions. Nature 332, 125–130.

Voight, B., 1989. A relation to describe rate-dependent material failure. Science 243, 200–203.

Walter, T.R., Acocella, V., Neri, M., Amelung, F., 2005. Feedback processes between magmatic events and flank movement at Mount Etna (Italy) during the 2002–2003 eruption. J. Geophys. Res. 110 (B10205). doi:10.1029/2005JB003688.

Waza, T., Kurita, K., Mizutani, H., 1980. The effect of water on the subcritical crack growth in silicate rocks. Tectonophysics 67, 25–34.

Whitten, C.A., 1956. Movement in California and Nevada. Trans. Am. Geophys. Union 37, 393–398.

Wiederhorn, S.M., Bolz, L.H., 1970. Stress corrosion and static fatigue of glass. J. Am. Ceram. Soc. 53, 543–548.

Wilson, B.M., 1989. Igneous Petrogenesis: A Global Tectonic Approach. Springer.

Wood, D.S., 1973. Patterns and magnitudes of natural strain in rocks. Philos. Trans. R. Soc. London 274, 373–382.

Wright, T.J., Ebinger, C., Biggs, J., Ayele, A., Yirgu, G., Keir, D., Stork, A., 2006. Magma-maintained rift segmentation at continental rupture in the 2005 Afar dyking episode. Nature 442, 291–294.

Wu, F.J., Thomsen, L., 1975. Microfracturing and deformation of Westerly granite under creep condition. Int. J. Rock Mech. Min. Sci. Geomech. Abstr., Abst. 12, 167–173.

Yang, S., Jiang, Y., 2010. Triaxial mechanical creep behaviour of sandstone. Min. Sci. Tech. 20, 339–349.